

Light propagation and gravitational lensing effects in charged Kalb–Ramond spacetime in nonlinear electrodynamics

C. F. S. Pereira,^{1,*} Marcos V. de S. Silva,^{2,†} A. R. Soares,^{3,‡}
A. A. Araújo Filho,^{4,5,6,§} R. L. L. Vitória,^{7,8,¶} and H. Belich^{1,**}

¹*Departamento de Física e Química, Universidade Federal do Espírito Santo,
Av. Fernando Ferrari, 514, Goiabeiras, Vitória, ES 29060-900, Brazil.*

²*Department of Theoretical Physics, Atomic and Optics, Campus Miguel Delibes,
University of Valladolid UVA, Paseo Belén, 7, 47011 - Valladolid, Spain*

³*Grupo de Investigação em Educação Matemática,
R. Dep. Gastão Vieira, 1000, CEP 65393-000 Buriticupu, MA, Brazil.*

⁴*Departamento de Física, Universidade Federal da Paraíba,
Caixa Postal 5008, 58051-970, João Pessoa, Paraíba, Brazil.*

⁵*Departamento de Física, Universidade Federal de Campina Grande Caixa Postal 10071,
58429-900 Campina Grande, Paraíba, Brazil.*

⁶*Center for Theoretical Physics, Khazar University,
41 Mehseti Street, Baku, AZ-1096, Azerbaijan.*

⁷*Programa de Pós-Graduação em Engenharia Aeroespacial, Universidade Estadual do Maranhão,
Cidade Universitária Paulo VI, São Luís 65055-310, MA, Brazil*

⁸*Faculdade de Física, Universidade Federal do Pará,
Av. Augusto Corrêa, Guamá, Belém, PA 66075-110, Brazil*

In this work, we theoretically investigate the deflection of light for strong- and weak-field regimes in the background of an electrically charged BH described in Kalb-Ramond gravity, which introduces the Lorentz symmetry violation parameter l , as well as the control of the degree of nonlinearity incorporated by electrodynamics through the parameter γ . We analytically constructed the expansion coefficients in both limits and used them as a basis to investigate gravitational lensing effects through observables, taking into account the variation of the parameters involved in the model, both for the canonical field and the phantom case.

* carlosfisica32@gmail.com

† marcos.sousa@uva.es

‡ adriano.soares@ifma.edu.br

CONTENTS

I. Introduction	2
II. Kalb-Ramond-ModMax spacetime and geodesic equations	4
III. Lensing phenomena	7
A. Expansion for light deflection in the weak-field limit	7
B. Deflection of light in the strong-field limit	12
IV. Lens equation and observables	16
A. Observables in the strong-field limit	18
B. Observables in the weak-field limit	23
V. Conclusion	25
Acknowledgments	26
References	26

I. INTRODUCTION

Singular black hole (BH) solutions arise naturally within the framework of general relativity (GR) as a result of the gravitational collapse process, being interpreted as the final stage of the stellar evolution of supermassive stars. The pioneering and most elementary theoretical formulation of these objects was presented by Karl Schwarzschild, consisting of a vacuum solution of the field equations established through Einstein's equations [1–4]. These geometric structures generally have as their main ingredients the emergence of event horizons and singularities, and for this configuration, which is the simplest geometry, all other quantities are defined as functions only of the mass parameter. A somewhat richer structure emerges in the construction of the Reissner-Nordström geometry, which, in a simplified way, describes an electrically charged BH. In this case, we have an electromagnetic vacuum, and in addition to the presence of a singularity and an event horizon, a new structure called the Cauchy horizon appears. This geometry, as with the Schwarzschild BH, is spherically symmetric and static; however, now all other quantities can be expressed in terms of the parameters of the mass M

§ dilto@fisica.ufc.br

¶ ricardovitoria@professor.uema.br/ricardo-luis91@hotmail.com

** humberto.belich@ufes.br

and the electric charge Q . These two geometries described above are extended to astrophysical scenarios through the stationary spacetimes of Kerr and Kerr–Newman [1, 2].

The static BH configuration supported by a Kalb-Ramond field was first constructed in Ref. [5]. Since its introduction, this geometry has motivated a broad range of investigations. Studies have examined its quasinormal spectra [6], transmission probabilities and greybody factors [7], quantum emission and evaporation processes [8], and gravitational deflection of light [9]. The orbital structure of test particles, including circular trajectories and quasi-periodic oscillations, has also been analyzed [10], as well as the accretion of collisionless Vlasov matter [11].

Subsequent developments generalized the original setup. A non-commutative deformation of the Kalb-Ramond BH has been proposed [12], extending the framework to incorporate short-distance corrections. In addition, an electrically charged counterpart was formulated in Ref. [13], followed by several works exploring its thermodynamic behavior, stability, and dynamical properties [14–18].

Further refinements revealed that the original construction did not exhaust the full solution space. Additional branches were identified in Refs. [19, 20], where previously overlooked configurations were systematically derived. These extended solutions have since been employed in different physical contexts, including analyses of entanglement degradation in curved backgrounds [21] and applications to neutrino propagation phenomena [22] for instance. Beyond these aspects, Kalb-Ramond gravity has been explored from several complementary perspectives. Investigations have addressed perturbative stability and phantom sectors [23], topological BHs in anti-de Sitter spacetimes [24], branching structures and non-extensive thermodynamics [25], as well as optical characteristics and particle dynamics [26], among other topics.

More recently, a distinct class of Kalb-Ramond BHs sourced by ModMax nonlinear electrodynamics has been introduced [23], with additional properties examined shortly thereafter [27]. Despite this growing body of work, a treatment of gravitational lensing in this ModMax-sourced scenario has not yet been carried out. The present study addresses this omission by providing a detailed analysis of light deflection in the corresponding geometry.

In Section II of this work, we present some general properties for the model as well as derive the conserved and geodesic quantities. In section III we analyze optical effects for the weak- and strong-field regimes. In Section IV we apply the gravitational lensing technique to the model and construct the observables. Finally, in Section V, we present the final considerations and conclusions.

II. KALB-RAMOND-MODMAX SPACETIME AND GEODESIC EQUATIONS

In this work, we will adopt the methodology used to calculate the deflection of light moving in a gravitational field and describing a spherically symmetric and static configuration for an electrically charged BH under the effects of Lorentz symmetry violation resulting from the coupling of nonlinear electrodynamics with Kalb-Ramond self-interaction fields, which was initially introduced by authors in Ref. [23]. This newly presented class of BH has already been explored in several scenarios, such as in the tidal force study where the authors investigate both radial and angular tidal forces on the event horizon, angular deviation, and the Roche limit [28]. These analyses were extended to particle dynamics, thermal properties, non-extensive thermodynamics, and observational signatures in Refs. [25, 27]. The line element of the metric describing the Kalb-Ramond-ModMax spacetime is given by [23]

$$ds^2 = -f(r)dt^2 + \frac{dr^2}{f(r)} + r^2 (d\theta^2 + \sin^2 \theta d\phi^2) , \quad (1)$$

where

$$f(r) = \frac{1}{1-l} - \frac{2M}{r} + \frac{\xi Q^2 e^{-\gamma}}{(1-l)^2 r^2} . \quad (2)$$

In the Eq. (2), the parameters M and Q represent the mass and electric charge of the BH, respectively. The effect associated with the violation of Lorentz symmetry arises naturally due to the presence of the antisymmetric Kalb-Ramond stress, which is associated with the expected non-zero vacuum value and is represented by the small parameter l . On the other hand, we have that the parameter γ is defined as positive and controls the degree of non-linearity of electromagnetism in such a way that when it tends to zero $\gamma \rightarrow 0$ Maxwell's electromagnetism is recovered, while the discrete parameter ξ determines whether the field is phantom $\xi = -1$ or canonical $\xi = 1$. The validity regime of the metric tensor coordinates is defined by: the coordinates t and r associated with the line element Eq. (1) and defined in Eq. (2) \in to the interval $(-\infty, \infty)$, $\theta \in [0, \pi)$ and $\phi \in [0, 2\pi)$. It is worth highlighting that, in the asymptotic regime, $f(r) \rightarrow 1 - \frac{l}{r-1}$. This implies that this metric describes a spacetime with a topological charge, just like in the global Monopole spacetime of Barriola and Vilenkin [29]. Thus, depending on the value of l , it is a space with an angular deficit/surplus effect, which influences photon propagation, as we will discuss later.

In a concise manner, we can define an expression to describe the position of the horizon structure, which is given below:

$$r_{H_{\pm}} = M(1-l) \left[1 \pm \sqrt{1 - \frac{\xi Q^2 e^{-\gamma}}{M^2(1-l)^3}} \right] , \quad (3)$$

where the positive sign represents the position of the event horizon r_{H_+} and the negative sign the Cauchy horizon r_{H_-} . By definition, for an event horizon to exist in the case of the BH with canonical field $\xi = 1$, the argument inside the square root must be positive and definite, imposing the following restriction among the system parameters $0 \leq Q \leq Me^{\gamma/2}(1-l)^{3/2}$. Note that we can rewrite the above constraint as $Q^2/M^2 \leq (1-l)^3 e^\gamma$ so that when the Lorentz violation parameters and the ModMax electrodynamics parameter cease to act $l = 0 = \gamma$, we then have the case of the extreme Reissner–Nordström BH $M = Q$ and the non-extreme $M > Q$ [30].

In order for the horizons to be well defined, two basic requirements must be satisfied: reality of the square root and positivity of the resulting radii. First, the reality condition demands

$$1 - \frac{\xi Q^2 e^{-\gamma}}{M^2(1-l)^3} \geq 0, \quad (4)$$

which can be rewritten as

$$\xi Q^2 e^{-\gamma} \leq M^2(1-l)^3. \quad (5)$$

Defining

$$\Delta \equiv 1 - \frac{\xi Q^2 e^{-\gamma}}{M^2(1-l)^3}, \quad (6)$$

the condition $\Delta \geq 0$ ensures that the horizons are real. The limiting case $\Delta = 0$ corresponds to an extremal configuration in which the two horizons coincide.

Second, the positivity of r_{H_\pm} requires that the overall prefactor $M(1-l)$ be positive. Assuming a positive mass parameter $M > 0$, this implies

$$1 - l > 0 \quad \iff \quad l < 1. \quad (7)$$

Under this condition, and provided $\Delta \geq 0$, both radii are non-negative. In particular, for $0 < \Delta < 1$, one has two distinct horizons,

$$r_{H_+} > r_{H_-} > 0, \quad (8)$$

whereas $\Delta = 0$ yields the degenerate (extremal) case

$$r_{H_+} = r_{H_-} = M(1-l). \quad (9)$$

If $\Delta < 0$, the square root becomes imaginary and no real horizons exist. Therefore, the necessary and sufficient conditions for real, positive event horizons are

$$M > 0, \quad \ell < 1, \quad \xi Q^2 e^{-\gamma} \leq M^2(1-l)^3. \quad (10)$$

Now, to study the deflection of light let us consider the geodesics of particles moving in the Kalb-Ramond-ModMax spacetime. Thus, we define a smooth curve in this spacetime, Eq. (1), that has length S which is given by

$$S = \int \sqrt{\left(g_{\mu\nu} \frac{dx^\mu}{d\lambda} \frac{dx^\nu}{d\lambda}\right)} d\lambda, \quad (11)$$

where λ is an affine parameter that can represent the observer's proper time. Taking S as the affine parameter itself, we can show that the curve that minimizes Eq. (11) is the same one that minimizes

$$\int \left(g_{\mu\nu} \frac{dx^\mu}{d\lambda} \frac{dx^\nu}{d\lambda}\right) d\lambda = \int \mathcal{L} d\lambda. \quad (12)$$

Therefore, considering the analysis in the equatorial plane, $\theta = \frac{\pi}{2}$, the Lagrangian becomes:

$$\mathcal{L} = -f(r) \left(\frac{dt}{d\lambda}\right)^2 + \frac{1}{f(r)} \left(\frac{dr}{d\lambda}\right)^2 + r^2 \left(\frac{d\phi}{d\lambda}\right)^2. \quad (13)$$

Applying the Euler-Lagrange equations to the above expression, we define the quantities conserved at time t and at ϕ . Therefore, we have to

$$L = r^2 \frac{d\phi}{d\lambda}, \quad E = f(r) \frac{dt}{d\lambda}. \quad (14)$$

Thus, substituting the conserved quantities, Eq. (14), in Eq. (13) and considering only null geodesics, $\mathcal{L} = 0$, it leads (13) to

$$\left(\frac{dr}{d\lambda}\right)^2 = \left[E^2 - \frac{L^2 f(r)}{r^2}\right]. \quad (15)$$

The expression above may be interpreted by analogy with the dynamics of a classical particle of unit mass, with energy \mathcal{E} , subject to an effective potential V_{eff} , given by

$$\mathcal{E} = E^2, \quad \text{and} \quad V_{\text{eff}} = \frac{L^2 f(r)}{r^2}. \quad (16)$$

In terms of Eq. (2), the effective potential becomes

$$V_{\text{eff}} = \frac{L^2}{r^2} \left(\frac{1}{1-l} - \frac{2M}{r} + \frac{\xi Q^2 e^{-\gamma}}{(1-l)^2 r^2} \right). \quad (17)$$

Radial motion is permitted only when $\mathcal{E} > V_{\text{eff}}$. In this context, we examine the situation in which the photon begins its trajectory in an asymptotically flat region and approaches a distance r_0 from the center of BH, reaching the so-called turning point, located outside the event horizon. As expected, once the photon reaches this limiting region, the gravitational field causes it to return toward another asymptotically flat region. At the turning point, one has, $V_{\text{eff}}(r_0) = E^2$, which, from Eq. (16), leads to

$$\frac{1}{\beta^2} = \frac{f(r_0)}{r_0^2}, \quad (18)$$

where $\beta = \frac{L}{E}$ is the impact parameter of the light ray. At the photon sphere radius, r_m , we have

$$\left. \frac{dV_{\text{eff}}}{dr} \right|_{r_m} = 0. \quad (19)$$

The critical impact parameter, β_c , is defined by the condition $\beta_c = \beta(r_m)$. Light rays with $\beta < \beta_c$ are completely absorbed, whereas those for which $\beta = \beta_c$ remain trapped on the photon sphere; in contrast, rays with $\beta > \beta_c$ are deflected and ultimately scattered. In the scattering regime, the deflection angle diverges in the limit $r_0 \rightarrow r_m$, which characterizes the so-called strong-field regime. In the following sections, we derive the approximation for the deflection angle in these two regimes, for this new class of electrically charged BH within the Kalb-Ramond theory.

Using Eq. (19) and Eq. (17), we can identify the position of the radius of the photon sphere, which is given in the expression below and has an inner r_{m1} and an outer radius r_{m2}

$$r_{m1} = \frac{3M(1-l)}{2} \left[1 - \sqrt{1 - \frac{8D}{9}} \right], \quad r_{m2} = \frac{3M(1-l)}{2} \left[1 + \sqrt{1 - \frac{8D}{9}} \right], \quad (20)$$

where the parameter above is defined as $D = \frac{\xi Q^2 e^{-\gamma}}{M^2(1-l)^3}$. Note that in the limit where the electric charge tends to zero $Q \rightarrow 0$ the radius of the photon sphere is recovered for the Schwarzschild BH, being deformed by the Lorentz symmetry violation parameter $r_{m2} = 3M(1-l)$ [31].

III. LENSING PHENOMENA

A. Expansion for light deflection in the weak-field limit

Considering light deflection in this scenario, with the line element and metric function defined by Eqs. (1) and (2) respectively, the expression for the impact parameter is obtained from Eq. (18) as follows:

$$\frac{1}{\beta^2(r_0)} = \frac{1}{r_0^2} \left[\frac{1}{(1-l)} - \frac{2M}{r_0} + \frac{(1-l)DM^2}{r_0^2} \right]. \quad (21)$$

In terms of Eq. (14), the radial equation Eq. (15) becomes

$$\left(\frac{dr}{d\phi} \right)^2 = r^4 \left[\frac{E^2}{L^2} - \frac{f(r)}{r^2} \right]. \quad (22)$$

Considering the symmetry that the distances before and after the inflection point are equal, we see that the contributions to the angular deviation are the same; therefore, we multiply the expression for the angular deviation by the factor 2;

$$\Delta\phi = \pm 2 \int_{r_0}^{\infty} \frac{dr}{r^2} \left[\frac{1}{\beta^2} - \frac{f(r)}{r^2} \right]^{-1/2}, \quad (23)$$

in developing this work, for the sake of symmetry, we only adopted the positive sign from the expression above. We now introduce a coordinate transformation in Eq. (23), where $u = \frac{1}{r}$. Note that, under this transformation, the integration limits become $u \rightarrow 0$ as $r \rightarrow \infty$, and $u \rightarrow u_0 = \frac{1}{r_0}$ as $r \rightarrow r_0$. Consequently, the equation for the angular deviation in the new coordinates takes the form

$$\Delta\phi = \int_0^{u_0} du \left[\frac{1}{\beta^2(r_0)} - \frac{u^2}{(1-l)} + 2Mu^3 - (1-l)DM^2u^4 \right]^{-1/2}. \quad (24)$$

Since our interest is in performing the angular deviation expansion of light in the weak-field regime, we must return to the expression for the impact parameter defined in Eq. (21) and then apply the same coordinate transformation introduced above, leading to the expression $\frac{1}{\beta^2} = u_0^2 \left[\frac{1}{(1-l)} - 2Mu_0 + (1-l)DM^2u_0^2 \right]$. Using this new form of the impact parameter and assuming that the photon travels away from the BH, we can adopt the approximation that both mass and electric charge are small parameters $M \ll 1$ and $Q \ll 1$. Consequently, expanding the orbital equation Eq. (24), up to the second order in M and charge Q , we find that the deflection of light is given by $\delta\phi = \Delta\phi - \pi$ and for the purposes of graphical analysis we will discard cross terms higher than the second order:

$$\begin{aligned} \delta\phi_{KR-ModMax} \approx & \pi \left(-1 + \sqrt{1-l} \right) + \frac{4M(1-l)^2}{\beta} + \frac{M^2(15\pi - 16)(1-l)^{7/2}}{4\beta^2} \\ & - \frac{\xi Q^2 e^{-\gamma}(1-l)^{1/2}}{32\beta^2} \left[24\pi + \frac{M(448 - 48\pi)(1-l)^{3/2}}{\beta} + \frac{25M^2(33\pi - 64)(1-l)^3}{\beta^2} \right]. \end{aligned} \quad (25)$$

In the expression above, we have the calculation of the light deviation for an electrically charged BH through nonlinear electrodynamics in the Kalb-Ramond theory, where the Lorentz symmetry violation effect is added through the non-zero expected vacuum value. Note that in the limit where the electric charge of the BH tends to zero $Q \rightarrow 0$, we obtain the angular deviation for the Schwarzschild BH being deformed by the Lorentz symmetry violation parameter, which also comes from Kalb-Ramond gravity and can be seen in the expression below:

$$\delta\phi_{Schwarzschild-like} \approx \pi \left(-1 + \sqrt{1-l} \right) + \frac{4M(1-l)^2}{\beta} + \frac{M^2(15\pi - 16)(1-l)^{7/2}}{4\beta^2}. \quad (26)$$

The expression for the simplified scenario above must be consistent with the light deviation in the field regime for a BH similar to that of Schwarzschild and analyzed in Ref. [31]. On the other hand, by also turning off the Lorentz symmetry violation effects $l \rightarrow 0$, we recover the light deviation for the Schwarzschild BH, and this result can be compared with several works obtained in the literature, and its reduced expression is given below

$$\delta\phi_{Schwarzschild} \approx \frac{4M}{\beta} + \frac{M^2(15\pi - 16)}{4\beta^2}. \quad (27)$$

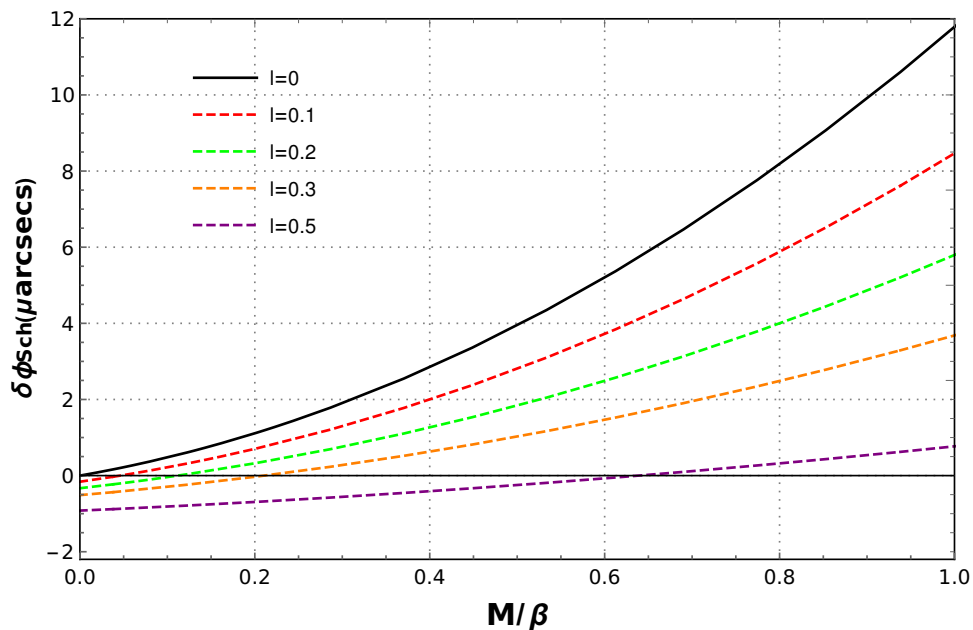


FIG. 1: Light deflection in the weak-field regime.

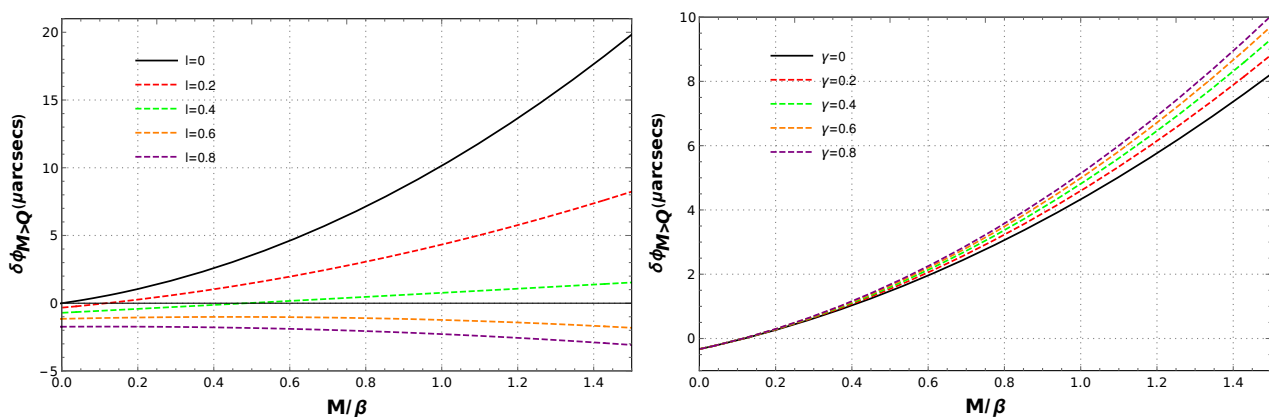


FIG. 2: In the figures above, we fix the parameter $\xi = 1$ and the mass $M = 1.2Q$. In the panel on the left, we consider $\gamma = 0$ and then vary l , while in the panel on the right we fix $l = 0.2$ and then vary γ .

Figure (1) provides a simplified illustration of weak-field light deflection for a Schwarzschild BH under Lorentz symmetry violation. This phenomenon, arising from Kalb-Ramond gravity, is governed by a parameter linked to a non-zero vacuum expectation value. Our results in Eq. (26) remain consistent with the optical analysis previously established in Ref. [31]. In the Fig. (1), the solid black curve corresponds to the standard Schwarzschild spacetime, while the dashed lines depict the influence of this vacuum-driven term. We observe that as this parameter increases positively, the angular deviation decreases, suggesting a potential attenuation of the spacetime curvature. This behavior is reversed for small negative values, in alignment with Refs. [30–32].

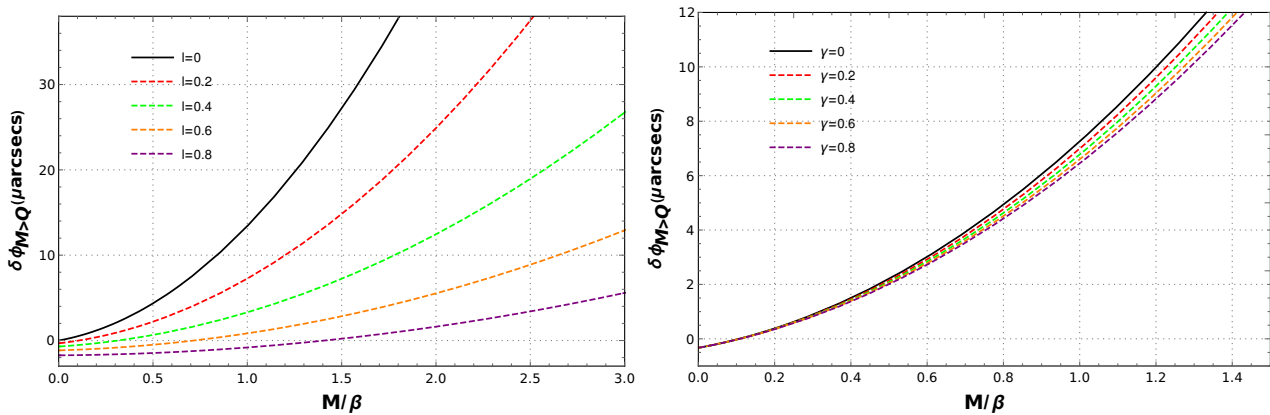


FIG. 3: In the figures above, we fix the parameter $\xi = -1$ and the mass $M = 1.2Q$. In the panel on the left, we consider $\gamma = 0$ and then vary l , while in the panel on the right we fix $l = 0.2$ and then vary γ .

In Figs. (2) and (3), we have, respectively, the representation of the non-extreme BH, where its mass has been fixed proportionally to the electric charge as $M = 1.2Q$, with the canonical field $\xi = 1$ and the phantom field $\xi = -1$. Thus, we can compare the panels on the left of Figs. (2) and (3), where we varied the Lorentz symmetry violation parameter and kept $\gamma = 0$. In both cases, the solid black curve represents the Schwarzschild BH and the dashed curves represent the deviation due to the influence of the Lorentz symmetry violation. In the upper left panel, we consider the canonical case and, in the lower left panel, the phantom case. Note in both left panels that for the curve corresponding to the parameter $l = 0.8$ in the phantom case, as the ratio M/β increases, the angular deviation is still positive, whereas for the canonical case, this deviation is negative for the same parameter value. Regarding the angular deviation for the phantom case (panel left of Fig. (3)), we can say that it is indeed a non-extreme BH, as the horizon radii assume real values for the chosen parameters. On the other hand, the angular deviation referring to the canonical case (panel left of Fig. 2), a transition occurs between the type of configuration, going from a non-extreme BH to a naked singularity, since the radius of the horizons for the parameter values initially chosen, being real as we vary the Lorentz symmetry violation parameter, gains an imaginary part.

On the other hand, in the panels on the right, in Figs. (2) and (3), we fixed the Lorentz symmetry violation parameter and then varied the parameter γ , which controls the nonlinearity of the electrodynamics. Thus, the solid black curve represents the angular deviation for $l = 0.2$, and the dashed curves show how this behavior occurs as we increase the nonlinearity in the model. Note that the behavior of the canonical field for the phantom case changes only due to a matter of symmetry with respect to the solid black reference curve. As mentioned above, the angular deviation graph on the right of Fig. (3) truly represents the non-extreme BH

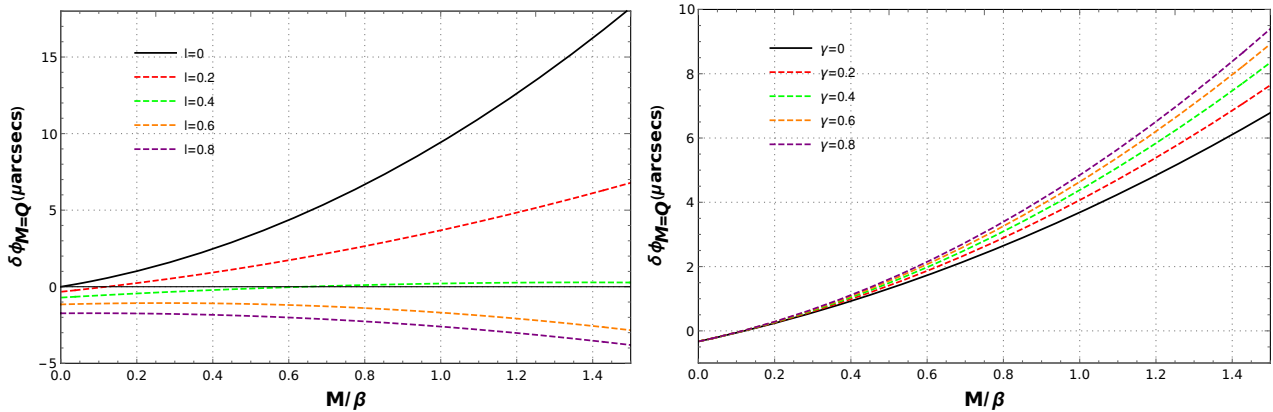


FIG. 4: In the figures above, we fix the parameter $\xi = 1$ and the mass $M = Q$. In the panel on the left, we consider $\gamma = 0$ and then vary l , while in the panel on the right we fix $l = 0.2$ and then vary γ .

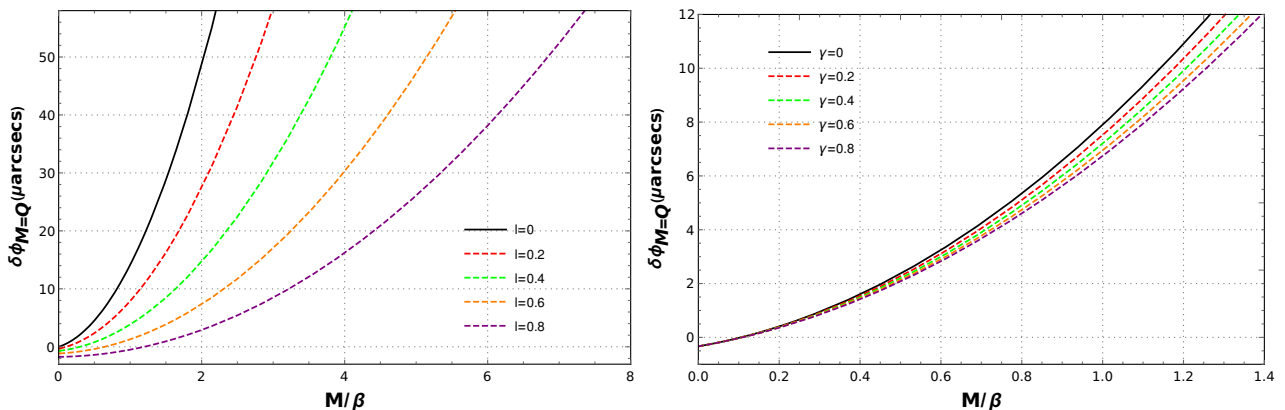


FIG. 5: In the figures above, we fix the parameter $\xi = -1$ and the mass $M = Q$. In the panel on the left, we consider $\gamma = 0$ and then vary l , while in the panel on the right we fix $l = 0.2$ and then vary γ .

configuration. Whereas for the canonical case (right of Fig. (2)) a transition occurs between a naked singularity and the non-extreme BH as we increase the value of γ .

Similar to the analysis performed for the non-extreme BH case, in the panels of Figs. (4) and (5) we perform the same procedure for the configuration $M = Q$, considering the canonical case and the phantom case. As we can see in these panels, the behavior of the angular deviations is similar to that of the case $Q < M$. Thus, for the canonical case (figure on the left of the panel (4)), a transition occurs between the case of an extreme BH and a naked singularity as we increase the parameter l and vice versa for the graph on the right. On the other hand, the phantom case represented by the panels in Fig. (5) shows the configurations for a non-extreme BH.

Finally, in Figs. (6) and (7) we have the graphical representation for the case $M < Q$. The

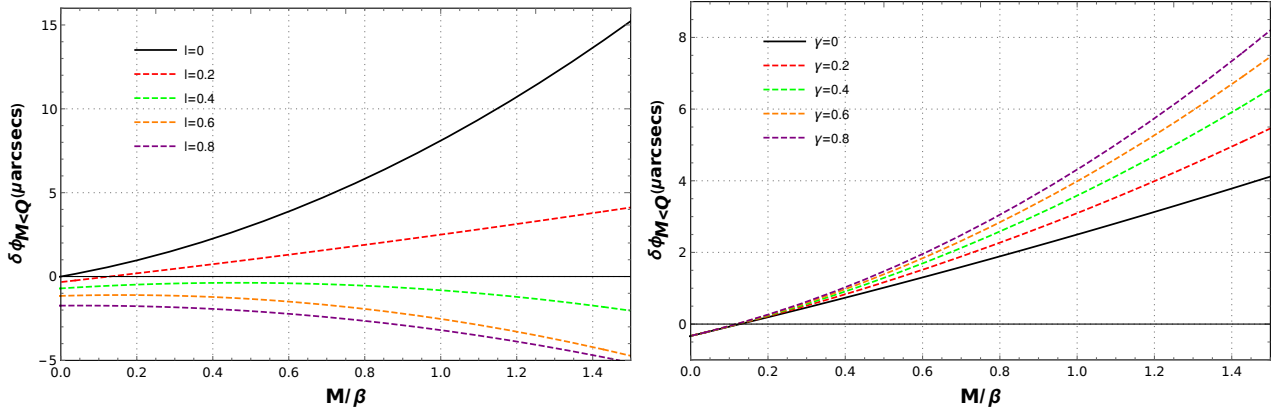


FIG. 6: In the figures above, we fix the parameter $\xi = 1$ and the mass $M = 0.8Q$. In the panel on the left, we consider $\gamma = 0$ and then vary l , while in the panel on the right we fix $l = 0.2$ and then vary γ .

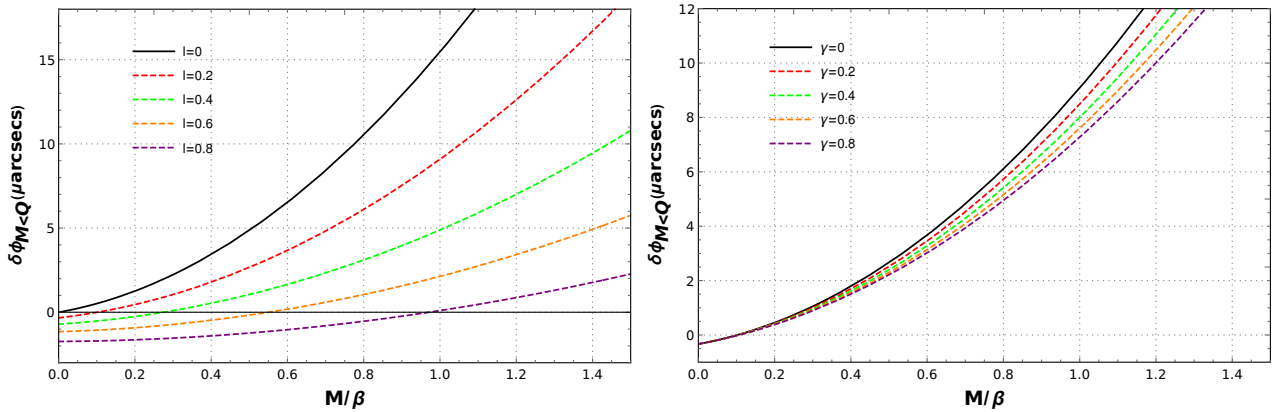


FIG. 7: In the figures above, we fix the parameter $\xi = -1$ and the mass $M = 0.8Q$. In the panel on the left, we consider $\gamma = 0$ and then vary l , while in the panel on the right we fix $l = 0.2$ and then vary γ .

figures in the first panel actually describe the characteristics of a naked singularity. However, the second panel, which represents the phantom system, despite the relation $M < Q$, as we vary the free parameters, the system assumes the characteristics of a non-extreme BH.

B. Deflection of light in the strong-field limit

In this section, our interest focuses on calculating the gravitational deflection of light in the strong-field regime, and for this, we will use as a basis the mechanism originally proposed by Bozza [33] and later improved by Tsukamoto [34]. In this context, we begin by transforming the variables $z = 1 - \frac{r_0}{r}$ into the orbit equation, Eq. (23), from which it can be expressed again as:

$$\Delta\phi(r_0) = \pm \int_0^1 \frac{2r_0 dz}{\sqrt{G(z, r_0)}}, \quad (28)$$

where

$$G(z, r_0) = \frac{r_0^4}{\beta^2} - \left(\frac{r_0^2}{1-l} \right) (1-z)^2 + 2Mr_0(1-z)^3 - (1-l)DM^2(1-z)^4. \quad (29)$$

After considering the series expansion of the function $G(z, r_0)$ at the point $z = 0$, which corresponds to the limit $r \rightarrow r_0$, we obtain that:

$$G(z, r_0) \simeq \Lambda_1(r_0)z + \Lambda_2(r_0)z^2, \quad (30)$$

where the expansion parameters Λ_1 and Λ_2 are defined as

$$\Lambda_1(r_0) = \frac{2(r_0 - r_{m1})(r_0 - r_{m2})}{1-l}, \quad \Lambda_1(r_0 \rightarrow r_{m2}) = 0, \quad (31)$$

$$\begin{aligned} \Lambda_2(r_0) &= -6DM^2(1-l) + r_0 \left(6M - \frac{r_0}{1-l} \right), \\ \Lambda_2(r_0 \rightarrow r_{m2}) &= \frac{1}{2} \left(-8D + 3\sqrt{9-8D} + 9 \right) (1-l)M^2. \end{aligned} \quad (32)$$

Considering the expansion coefficients contained in Eqs. (31) and (32) for the strong-field regime $r \rightarrow r_m$, and analyzing the integration expression of Eq. (28), a logarithmic divergence is observed and, therefore, it is necessary to separate this integral into two parts: a regular part $\Delta\phi_R(r_0)$ and a divergent part $\Delta\phi_D(r_0)$. Thus, we have:

$$\Delta\phi(r_0) = \Delta\phi_R(r_0) + \Delta\phi_D(r_0). \quad (33)$$

Thus, the divergent part of the integration is defined as

$$\begin{aligned} \Delta\phi_D(r_0) &= \int_0^1 \frac{2r_0}{\sqrt{\Lambda_1(r_0)z + \Lambda_2(r_0)z^2}} = -\frac{4r_0}{\sqrt{\Lambda_2(r_0)}} \log \left(\sqrt{\Lambda_1(r_0)} \right) \\ &+ \frac{4r_0}{\sqrt{\Lambda_2(r_0)}} \log \left(\sqrt{4\Lambda_2(r_0)} \right) = -\frac{2r_0}{\sqrt{\Lambda_2(r_0)}} \log (\Lambda_1(r_0)) + \frac{2r_0}{\sqrt{\Lambda_2(r_0)}} \log (4\Lambda_2(r_0)). \end{aligned} \quad (34)$$

To control the way the integration divergence occurs, we need to expand the coefficient $\Lambda_1(r_0)$ and the impact parameter $\beta(r_0)$ when the radius of the distant photon approaches the outer radius of the photon sphere $r_0 \rightarrow r_{m2}$. Thus, Eqs. (19) and (23) become:

$$\beta(r_0) \simeq \frac{1}{\sqrt{8\eta}} + \frac{\left(9 - 8D + 3\sqrt{9-8D} \right) \left(r_0 - r_{m2} \right)^2}{\sqrt{2} \left(3 + \sqrt{9-8D} \right)^6 \left(1-l \right)^5 M^4 \eta^{3/2}}, \quad (35)$$

where the parameter η is defined as being

$$\eta = \frac{(3 - 2D + \sqrt{9 - 8D})}{(3 + \sqrt{9 - 8D})^4 M^2 (1 - l)^3}. \quad (36)$$

Thus, we can use the expression for the expanded impact parameter above Eq. (35) and then substitute it into the expansion coefficient of Eq. (31) to consider that this photon, coming from infinity, approaches the outer radius of the photon sphere even further. Therefore, the expansion coefficient in this limit is given by

$$\begin{aligned} \Lambda_1(r_0 \rightarrow r_{m2}) \simeq 6M \sqrt{1 - \frac{8D}{9}} \left[\frac{(3 + \sqrt{9 - 8D})^6 M^4 \eta (1 - l)^5}{2(9 - 8D + 3\sqrt{9 - 8D})} \right]^{1/2} \times \\ \left[\beta \sqrt{\frac{8(3 - 2D + \sqrt{9 - 8D})}{(3 + \sqrt{9 - 8D})^4 M^2 (1 - l)^3} - 1} \right]^{1/2}. \end{aligned} \quad (37)$$

Then, substituting equations (32), (35) and (37) into expression (34), with some algebraic manipulation, we obtain the divergent part related to the integration of the angular deviation:

$$\begin{aligned} \Delta\phi_D = -\sqrt{\frac{(3 + \sqrt{9 - 8D})(1 - l)}{2\sqrt{9 - 8D}}} \log \left[\beta \sqrt{\frac{2(1 + \sqrt{9 - 8D})}{(3 + \sqrt{9 - 8D})^3 M^2 (1 - l)^3} - 1} \right] \\ + \sqrt{\frac{(3 + \sqrt{9 - 8D})(1 - l)}{2\sqrt{9 - 8D}}} \log \left[\frac{8\sqrt{9 - 8D}}{1 + \sqrt{9 - 8D}} \right]. \end{aligned} \quad (38)$$

The expression constructed above refers to the divergent part of the integration of the angular deviation. Regarding the contribution from the regular part, since this integration cannot be done analytically, we will therefore treat it numerically. Thus, the regular part is given by

$$\Delta\phi_R = \int_0^1 \left(\frac{2r_{m2} dz}{\sqrt{G(z, r_{m2})}} \right) - \int_0^1 \left(\frac{2r_{m2} dz}{\sqrt{\Lambda_2(r_{m2}) z}} \right). \quad (39)$$

Therefore, the total deviation of light due to the presence of the gravitational field in this electrically charged BH in Kalb-Ramond gravity is defined as $\delta\phi = \Delta\phi_D + \Delta\phi_R - \pi$. Since the expression for the regular part of the integration does not have an analytical solution, we will perform the numerical treatment. In a simplified manner, and to verify the effectiveness of the methodology discussed, we can observe in Fig. (8) the representation of the angular deviation suffered by a beam of light for the Schwarzschild BH when subjected to the effects of Kalb-Ramond gravity. Note that in the panel on the left of this figure we consider positive values of the violation parameter, while in the panel on the right we adopt negative values;

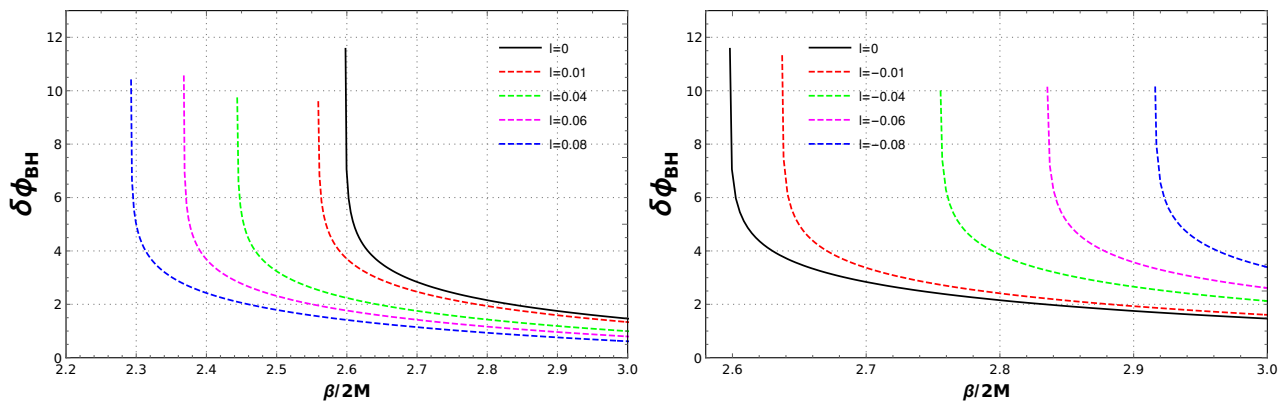


FIG. 8: Angular deflection for a Schwarzschild-type BH in Kalb-Ramond gravity.

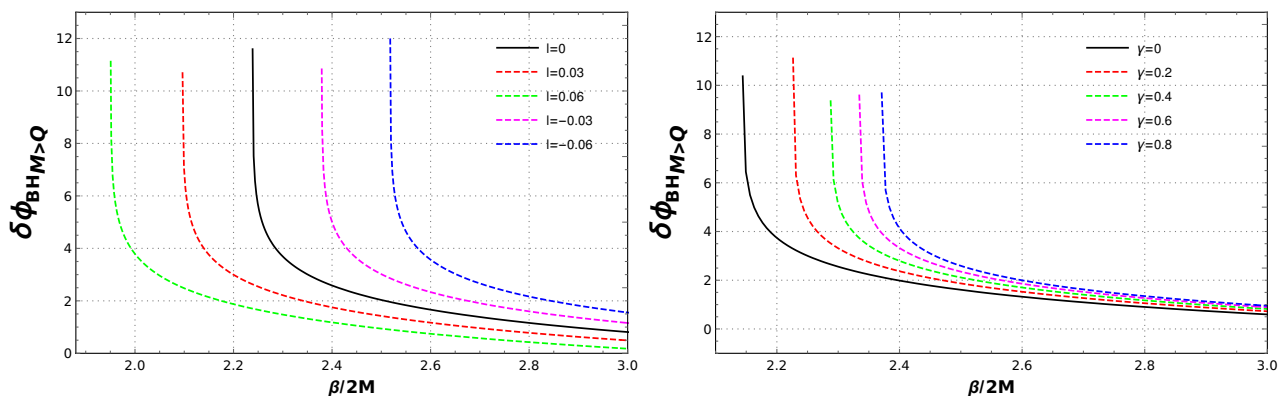


FIG. 9: Angular deflection of light for a BH in Kalb-Ramond gravity, where in the panel on the left we fix the parameters $\xi = 1$ and $\gamma = 0$ and then vary l . In the panel on the right we fix $l = 0.02$ and $\xi = 1$ and then vary the parameter γ .

what changes from one to the other is the intensity of the curvature in the vicinity of the BH, contributing to amplifying or attenuating the effect.

In panels of Figs. (9) and (10) we can observe the gravitational deviation for an electrically charged BH subjected to Kalb-Ramond gravity. In both panels, we are considering only the case of the usual BH where mass is greater than the amount of electric charge; for our analysis, we are considering $M = 1.2Q$, so that in the first panel (9) we are considering the case where the field is canonical, and the second is the same analysis for the phantom field (10). In particular, we can observe in the panel on the left of the Fig. (9) that we are considering the scenario where the parameter controlling the degree of non-linearity of the electrodynamics is fixed $\gamma = 0$ and then we are analyzing the situation when the Lorentz symmetry violation parameter is modifying the light deviation for the case $l = 0$ (black continuous curve). Note that we adopt positive and negative values for this parameter, which may indicate amplification or attenuation of the angular deviation. On the other hand, in the panel to the right of the Fig. (9) the continuous black curve represents the angular deviation of the light for the Lorentz symmetry violation

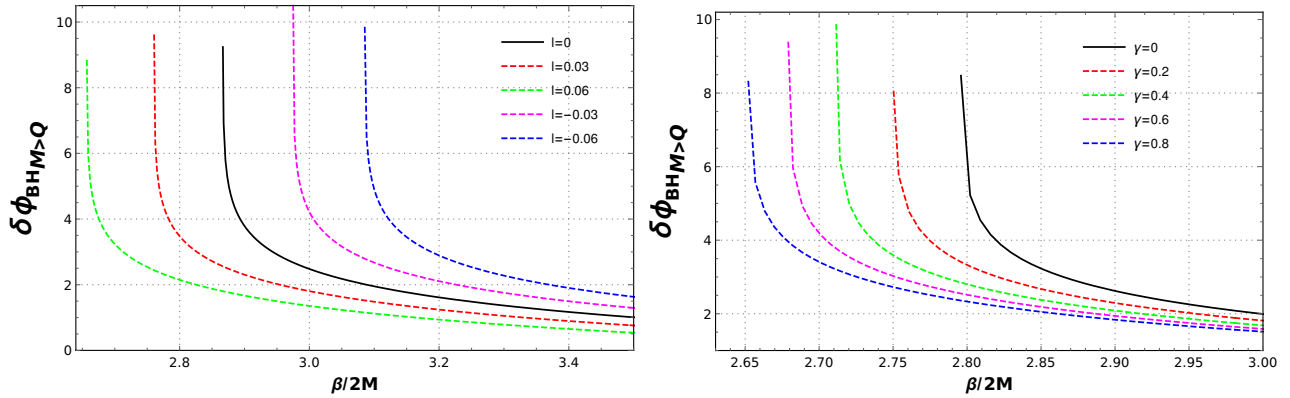


FIG. 10: Angular deflection of light for a BH in Kalb-Ramond gravity, where in the panel on the left we fix the parameters $\xi = -1$ and $\gamma = 0$ and then vary l . In the panel on the right we fix $l = 0.02$ and $\xi = -1$ and then vary the parameter γ .

parameter set at $l = 0.02$ and then we are varying the non-linearity parameter, which in this usual case plays the role of amplifying the angular deviation and in the phantom case (panel to the right of the Fig. (10)) it reduces the deviation. Finally, if we compare the panels to the left of Figs. (9) and (10), which show the canonical case and the phantom respectively, what changes from one behavior to the other is only a shift in the coordinate represented by the ratio $\beta/2M$.

IV. LENS EQUATION AND OBSERVABLES

In this section, we will construct the connection between the angle of deflection of light in the weak-field regime Eq. (25), and in the strong-field regime, Eqs. (38) and (39), with $\delta\phi = \Delta\phi_R + \Delta\phi_D - \pi$, using the master equations of gravitational lensing as a starting point. In this way, we can construct physical quantities that can be theoretically associated with observables. Considering the strong-field regime as a starting point.

Figure (11) illustrates the gravitational lensing diagram. Thus, the light beam emitted by the source \mathbf{S} is deflected due to the presence of the BH located at \mathbf{L} and subsequently propagates towards the observer \mathbf{O} . The angular deviation of the light deflection is denoted by α . The angular positions of the source and the image relative to the optical axis, \overline{LO} , are represented by ψ and θ , respectively. Thus, considering that the source \mathbf{S} is practically aligned with the lens \mathbf{L} , a position in which the relativistic images should be more expressive [35, 36], we then have the lens equation that relates the angular positions ψ and θ defined as

$$\psi = \theta - \frac{D_{LS}}{D_{OS}} \Delta\alpha_n, \quad (40)$$

where $\Delta\alpha_n$ is the deflection angle subtracted from all the loops made by the photons before

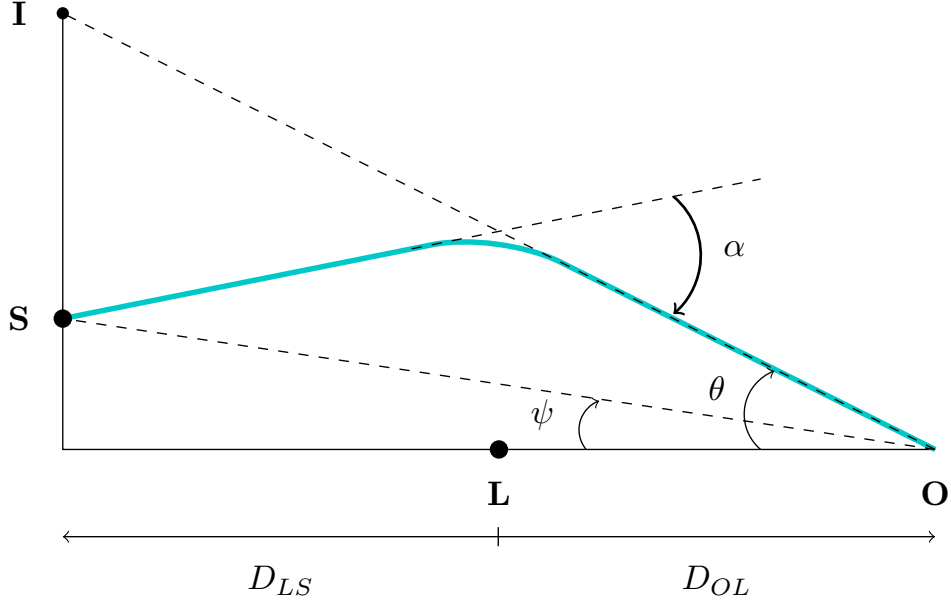


FIG. 11: Light angular deflection diagram.

reaching the observer, that is, $\Delta\alpha_n = \alpha - 2n\pi$. In this approach, we use the following approximation for the impact parameter $\beta \approx \theta D_{OL}$. Then the contributions to the angular deflection, Eqs. (38) and (39), are rewritten as:

$$\alpha(\theta) = -\bar{a} \log \left(\frac{\theta D_{OL}}{\beta_c} - 1 \right) + \bar{b}, \quad (41)$$

where we have

$$\beta_c = \sqrt{\frac{(3 + \sqrt{9 - 8D})^3 M^2 (1 - l)^3}{2(1 + \sqrt{9 - 8D})}}, \quad \bar{a} = \sqrt{\frac{(3 + \sqrt{9 - 8D})(1 - l)}{2\sqrt{9 - 8D}}}, \quad (42)$$

$$\bar{b} = \sqrt{\frac{(3 + \sqrt{9 - 8D})(1 - l)}{2\sqrt{9 - 8D}}} \log \left[\frac{8\sqrt{9 - 8D}}{1 + \sqrt{9 - 8D}} \right] + \Delta\phi_R - \pi, \quad (43)$$

given that the regular part is given by Eq. (39).

To obtain $\Delta\alpha_n$, we expand $\alpha(\theta)$ close to $\theta = \theta_n^0$, where $\alpha(\theta_n^0) = 2n\pi$, and find that

$$\Delta\alpha_n = \left. \frac{\partial\alpha}{\partial\theta} \right|_{\theta=\theta_n^0} (\theta - \theta_n^0). \quad (44)$$

Evaluating Eq. (41) on $\theta = \theta_n^0$, we have

$$\theta_n^0 = \frac{\beta_c}{D_{OL}} (1 + e_n), \quad \text{with } e_n = e^{\frac{\bar{b} - 2n\pi}{\bar{a}}}. \quad (45)$$

Substituting Eq. (41) and (45) in Eq. (44), we have

$$\Delta\alpha_n = -\frac{\bar{a} D_{OL}}{\beta_c e_n} (\theta - \theta_n^0). \quad (46)$$

Therefore, substituting Eq. (46) into Eq. (40) and performing some algebraic manipulations, we obtain the expression for the angular position of the lens:

$$\theta_n \approx \theta_n^0 + \left(\frac{e_n \beta_c}{\bar{a}} \right) \frac{D_{OS}(\psi - \theta_n^0)}{D_{OL} D_{LS}}. \quad (47)$$

Although the deflection of light preserves the surface brightness of the source, the gravitational lensing phenomenon alters the solid angle at which this source is perceived by the observer. Consequently, the total observed flux of an image subject to the gravitational lensing effect is proportional to the magnification factor μ_n , which is defined by $\mu_n = \left| \frac{\psi}{\theta} \frac{\partial \psi}{\partial \theta} \Big|_{\theta=\theta_n^0} \right|^{-1}$. Therefore, substituting Eq. (40) into Eq. (46), we have

$$\mu_n = \frac{e_n(1 + e_n)}{\psi \bar{a}} \left(\frac{\beta_c}{D_{OL}} \right)^2 \frac{D_{OS}}{D_{LS}}. \quad (48)$$

The magnification decreases sharply with increasing n , implying that the brightness of the first image, θ_1 , predominates over that of subsequent images. Furthermore, the presence of the factor $\left(\frac{\beta_c}{D_{OL}} \right)^2$ indicates that the magnification remains intrinsically small. It is further observed that, in the limit $\psi \rightarrow 0$, corresponding to the maximum alignment between the source, the lens, and the observer, the magnification diverges, resulting in a significant increase in the probability of detecting relativistic images.

A. Observables in the strong-field limit

In the previous sections, the positions of the relativistic images, as well as their respective fluxes, were determined as a function of the expansion parameters \bar{a} , \bar{b} , and β_c . At this point, we adopt the inverse procedure, reconstructing the expansion coefficients from observational data. This approach allows us to investigate the properties of the object responsible for the gravitational lensing effect and, subsequently, to compare the observational results with the corresponding theoretical predictions. The impact parameter can be expressed in terms of θ_∞ [33],

$$\beta_c = D_{OL} \theta_\infty. \quad (49)$$

We will follow Bozza [33] and assume that only the outermost image θ_1 is resolved as a single image while the others are encapsulated in θ_∞ . Thus, Bozza defined the following observables,

$$s = \theta_1 - \theta_\infty = \theta_\infty e^{\frac{\bar{b}-2\pi}{\bar{a}}}, \quad (50)$$

$$\tilde{r} = \frac{\mu_1}{\sum_{n=2}^{\infty} \mu_n} = e^{\frac{2\pi}{\bar{a}}}, \quad (51)$$

where the parameters \bar{a} and \bar{b} are defined in the expressions (42) and (43).

In the previous expressions, \mathbf{s} represents the angular separation, while \tilde{r} characterizes the ratio between the flux of the first image and that of the subsequent images. These relationships can be inverted in order to determine the corresponding expansion coefficients. For the analysis of the observables, we assume that the object under consideration has an estimated mass of $4.4 \times 10^6 M_\odot$ and is located at an approximate distance of $D_{OL} = 8.5 \text{Kpc}$, values comparable to those associated with the BH at the center of our galaxy [37]. In geometric units, we have the rescaling of the mass to $M \rightarrow \frac{MG}{c^2}$ and $\theta_\infty = 26.5473 \mu\text{arcsecs}$, which is the same used for the Schwarzschild BH.

In TABLE I we have assigned the variation of the Lorentz symmetry violation parameter to verify how it modifies observables such as the angular separation \mathbf{s} , the parameter associated with the flux of the first image \mathbf{r} and the angular position at infinity, referring to the Schwarzschild BH and considering the data for the BH at the center of our galaxy and already described in the previous paragraph. The data presented in this table for the angular separation can be visualized in the panel on the left, through the dashed blue curve in the graph of Fig. (12) and show how this result deviates from the curve referring to the Schwarzschild BH (solid black curve). Note that, as the Lorentz violation parameter approaches $l \rightarrow 1$, the angular separation approaches zero, as we can see in the third column of the table I. On the other hand, on the right side of Fig. (12) we have the graphical representation of what the flux of the first image would be growing as the Lorentz violation parameter tends to ≈ 1 (dashed red curve) compared to the Schwarzschild BH (solid black curve).

TABLE I: Observable quantities as functions of the Lorentz violation parameter l for the Schwarzschild BH.

l	θ_∞ (μ arcsecs)	s (μ arcsecs)	$r = 2.5 \log_{10} \tilde{r}$ (magnitudes)
-0.6	0.00026	0.23915	5.39317
-0.4	0.00021	0.14297	5.76554
-0.1	0.00017	0.07552	6.22750
0.0	0.00013	0.03322	6.82188
0.1	0.00009	0.01092	7.62710
0.4	0.00006	0.00214	8.80701
0.6	0.00003	0.00014	10.78630

In tables II and III we construct data for some observables for the non-extreme BH, taking into account the BH data at the center of our galaxy and, respectively, considering the case where the field is canonical $\xi = 1$ and the phantom case $\xi = -1$. In this way, we kept

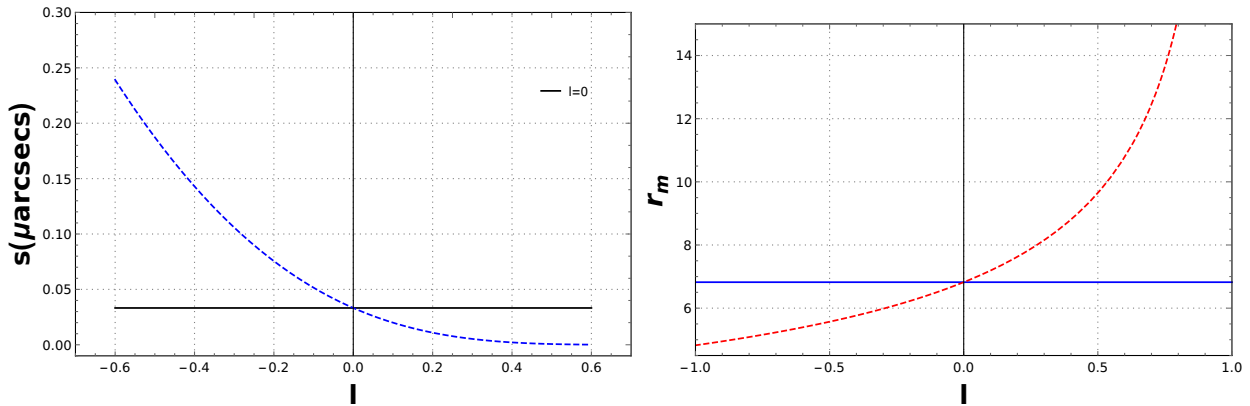


FIG. 12: Angular separation and $2.5 \log_{10} \bar{r}$ as a function of the Lorentz symmetry violation parameter for the Schwarzschild BH.

TABLE II: Observable quantities as a function of the Lorentz violation parameter l for the electrically charged non-extreme case BH. We fix the parameters $\xi = 1$ and $\gamma = 0$.

l	ξ	γ	θ_{∞} (μ arcsecs)	s (μ arcsecs)	$r = 2.5 \log_{10} \bar{r}$ (magnitudes)
-0.10	1	0	0.000134	0.08504	5.98069
-0.06	1	0	0.000125	0.07951	5.99791
-0.02	1	0	0.000116	0.07607	5.98658
0.0	1	0	0.000111	0.07543	5.96435
0.02	1	0	0.000106	0.07580	5.92588
0.06	1	0	0.000097	0.08147	5.77078
0.10	1	0	0.000087	0.10321	5.39397

TABLE III: Observable quantities as a function of the Lorentz violation parameter l for the electrically charged non-extreme case BH. We fix the parameters $\xi = -1$ and $\gamma = 0$.

l	ξ	γ	θ_{∞} (μ arcsecs)	s (μ arcsecs)	$r = 2.5 \log_{10} \bar{r}$ (magnitudes)
-0.10	-1	0	0.000160	0.03798	6.80626
-0.06	-1	0	0.000153	0.03093	6.92208
-0.02	-1	0	0.000146	0.02481	7.12969
0.0	-1	0	0.000142	0.02208	7.21835
0.02	-1	0	0.000139	0.01956	7.31051
0.06	-1	0	0.000132	0.01512	7.50619
0.10	-1	0	0.000125	0.01144	7.71864

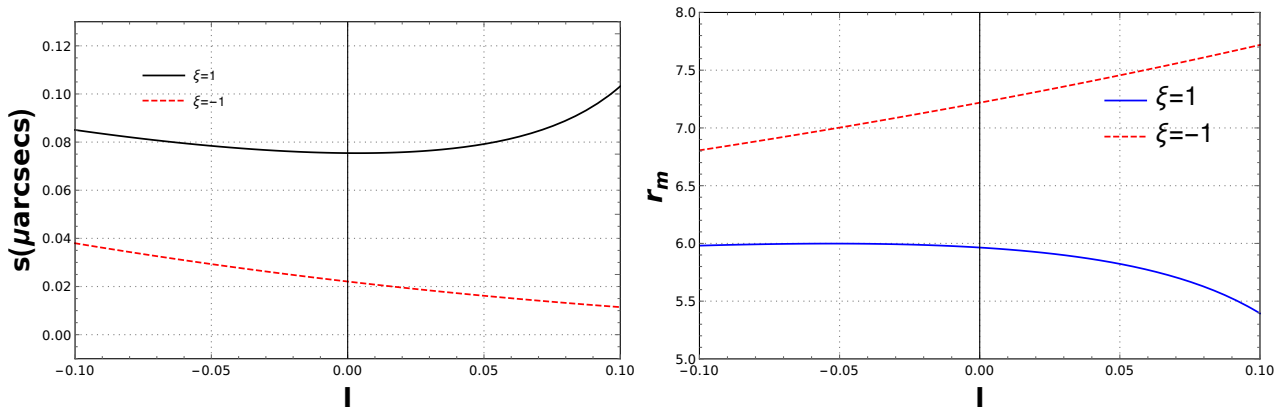


FIG. 13: Angular separation and $2.5 \log_{10} \bar{r}$ as a function of the Lorentz symmetry violation parameter for the electrically charged non-extreme BH.

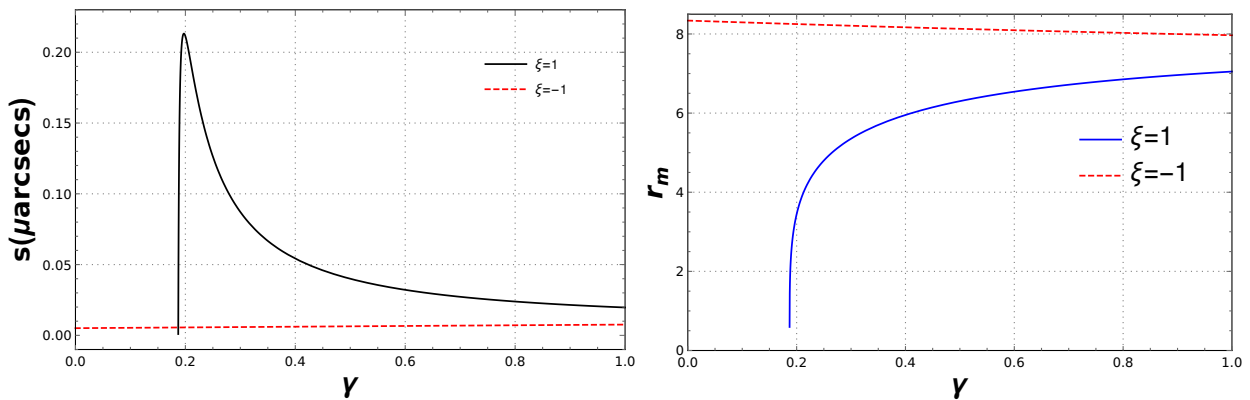


FIG. 14: Angular separation and $2.5 \log_{10} \bar{r}$ as a function of the parameter γ for the electrically charged non-extreme BH.

the parameter that regulates nonlinearity fixed $\gamma = 0$ and then varied the Lorentz symmetry violation parameter.

For illustrative purposes, the data contained in these tables for angular separation and the relationship of the flow of the first image with the others can be visualized through the panels found in the Fig. (13). Thus, note in the continuous black curve (on the left) that the angular separation for the canonical field case reaches a minimum point and then increases again, a behavior that is consistent with table II. However, for the phantom case (red dotted curve on the left), the angular separation continues to decrease as the Lorentz violation parameter approaches $l \approx 0.1$ and this behavior is in accordance with the table III. In the panel to the right of the Fig. (13), we can observe that in the continuous blue curve, the flux ratio of the first image to the others reaches a maximum value and then begins to decrease as the Lorentz symmetry violation parameter approaches $l \approx 0.1$. This behavior is consistent with the data contained in table II. On the other hand, this same quantity for the phantom case (dashed red

TABLE IV: Observable quantities as a function of the parameter controlling the nonlinearity γ for the non-extreme case of an electrically charged BH. We fix the parameters $\xi = 1$ and $l = 0.2$.

l	ξ	γ	θ_∞ (μ arcsecs)	s (μ arcsecs)	$r = 2.5 \log_{10} \bar{r}$ (magnitudes)
0.2	1	0.2	0.000066	0.21134	3.44546
0.2	1	0.4	0.000074	0.05424	5.95292
0.2	1	0.6	0.000078	0.03214	6.54114
0.2	1	0.8	0.000081	0.02389	6.85321
0.2	1	0.9	0.000082	0.02149	6.96180
0.2	1	0.95	0.000083	0.02052	7.00826
0.2	1	0.98	0.000083	0.02000	7.03405

TABLE V: Observable quantities as a function of the parameter controlling the nonlinearity γ for the non-extreme case of an electrically charged BH. We fix the parameters $\xi = -1$ and $l = 0.2$.

l	ξ	γ	θ_∞ (μ arcsecs)	s (μ arcsecs)	$r = 2.5 \log_{10} \bar{r}$ (magnitudes)
0.2	-1	0.2	0.000107	0.00559	8.24997
0.2	-1	0.4	0.000104	0.00611	8.16849
0.2	-1	0.6	0.000102	0.00663	8.09435
0.2	-1	0.8	0.000101	0.00713	8.02769
0.2	-1	0.9	0.000100	0.00736	7.99716
0.2	-1	0.95	0.000099	0.00748	7.98258
0.2	-1	0.98	0.000099	0.00755	7.97405

curve) shows an increasing behavior in this interval and can be observed in table III.

In tables IV and V, we constructed data for some observables related to the non-extreme BH, taking into account the BH data at the center of our galaxy and, respectively, considering the case where the field is canonical $\xi = 1$ and the phantom case $\xi = -1$. In this way, we fixed the Lorentz symmetry violation parameter $l = 0.2$ and then varied the parameter that controls the nonlinearity. We have created a graphical representation of how varying the parameter that controls nonlinearity is modifying the angular separation and magnification associated with the image flow, which can be seen in Fig. (14).

In the red dotted panel on the left of Fig. (14), the angular separation assumes slightly increasing values for the phantom case, as the nonlinearity parameter tends to $\gamma \rightarrow 1$, in accordance with table V. In the case where the field is canonical (black continuous curve), the angular separation reaches a maximum point at $\gamma \approx 0.19$, and then this quantity begins to have an imaginary contribution that does not appear in the table IV, since the smallest value chosen was $\gamma = 0.2$.

In the panel on the right of the Fig. (14) dotted red curve, we have the curve that relates the flow in the first image with the others for the phantom field and note that it decreases as the nonlinearity parameter tends to $\gamma \rightarrow 1$, a behavior that is in accordance with the data presented in the table V. On the other hand, for the canonical case (continuous blue curve), this quantity tends to increase as the parameter approaches $\gamma \rightarrow 1$ and is consistent with the table IV. However, for the value of the parameter $\gamma \approx 0.19$, this quantity, as well as the angular separation (continuous black curve on the left), begins to have an imaginary contribution.

B. Observables in the weak-field limit

The next step is to analyze the observables in the weak-field regime, which means that the impact parameter is very large relative to the object's mass, $\beta \gg M$, so that the light beam does not form loops. We can also note that for simplicity we will develop this analysis considering only a Schwarzschild-type BH contained within Kalb-Ramond gravity, so as to consider only the linear term in the mass M . Therefore, the expression Eq. (23) becomes

$$\delta\phi \sim \pi \left(-1 + \sqrt{1-l} \right) + \frac{4M(1-l)^2}{\beta}. \quad (52)$$

Taking as a starting point the equation that relates the angular positions of the source and the image, Eq. (40), we analyze the particular case of perfect alignment between the source, the compact object, and the observer, a situation that corresponds to the limit $\psi = 0$. In this way, we have to

$$\theta = \frac{D_{LS}}{D_{OS}} \Delta\alpha_n, \quad (53)$$

where $\Delta\alpha_n$ is given by Eq. (52). Therefore, substituting Eq. (52) into Eq. (53) and keeping only terms up to first order in the mass M , we obtain a second-degree algebraic equation, which when solved gives us the angular position θ_E for the Einstein ring:

$$\begin{aligned} \theta = \theta_E = & \frac{D_{LS} \pi \left(-1 + \sqrt{1-l} \right)}{2 D_{OS}} \\ & + \frac{1}{2} \left[\frac{D_{LS}}{D_{OS}} \left(\frac{D_{LS}}{D_{OS}} \left(\pi \left(-1 + \sqrt{1-l} \right) \right)^2 + \frac{16 M (1-l)^2}{D_{OL}} \right) \right]^{1/2}. \end{aligned} \quad (54)$$

Thus, in the expression above we can clearly observe that the Lorentz symmetry violation parameter, as well as the mass of the Schwarzschild BH, is modifying the relative position of the Einstein ring. In this sense, we can also point out that, as observed in the light deflection in both weak- and strong-field regimes, the position of the Einstein ring varies depending on whether we are considering the violation parameter with positive or negative values. From the expression above regarding the angular position of the Einstein ring, we can consistently recover the expression referring to the Schwarzschild BH when the effects of Lorentz symmetry violation are deactivated $l \rightarrow 0$ [38]:

$$\theta = \theta_E = \sqrt{\frac{4MD_{LS}}{D_{OS}D_{OL}}}. \quad (55)$$

We can also calculate the radius of the Einstein ring from the approximation $\beta \approx \theta D_{OL}$ and using Eq. (54) [38, 39]. Therefore, we have

$$R_E = D_{OL}\theta_E. \quad (56)$$

Therefore, observables R_E and θ_E can be determined by considering different values of the parameter l , associated with the violation of the Lorentz symmetry, as well as the mass M . Within the scope of this analysis, restricted to the weak-field regime, we investigate the gravitational lensing effect, taking as an example a star located in the galactic bulge [40]. To this end, we consider the following values for the parameters $D_{OL} = 4Kpc$ and $D_{OS} = 8Kpc$.

TABLE VI: Radius of the Einstein ring and angular position as a function of the Lorentz violation parameter l .

l	R_E (km)	θ_E (arcsecs)
-0.6	5.14×10^{16}	85831.20
-0.4	3.55×10^{16}	59362.00
-0.1	9.46×10^{15}	15814.1
0.0	1.27×10^{12}	2.12
0.1	1.31×10^8	2.2×10^{-4}
0.4	1.32×10^7	2.2×10^{-5}
0.6	3.60×10^6	6.02×10^{-6}

In table VI we have collected numerical data for both the angular position and the radius of the Einstein ring, taking into account the Schwarzschild BH which is deformed by the Lorentz symmetry violation parameter l . Thus, note that as the Lorentz symmetry violation parameter

increases $l \approx 1$, both the angular position and the radius of the Einstein ring decrease. To verify the consistency in the data construction, note that the values of these quantities for Schwarzschild BH $l = 0$, are in agreement with those obtained in previous studies [38, 41].

V. CONCLUSION

In this work, we initially establish the general relationships and conserved quantities, as well as the geodesic trajectories, for an electrically charged beam subjected to Kalb-Ramond gravity that incorporates the Lorentz symmetry violation parameter. Subsequently, we focus on investigating the gravitational deflection of a light beam when subjected to the weak-field regime. To verify the consistency of the methodology employed, we obtained the gravitational shift for the most general background investigated, and then we found the angular shift for a more simplified background Eq. (25), which would be the Schwarzschild BH in the Kalb-Ramond theory Eq. (26), as well as the shift referring only to the Schwarzschild BH when considering that the Lorentz symmetry violation effects were turned off $l \rightarrow 0$ Eq. (27). We constructed graphical representations to analyze the relationship between mass and electric charge parameters, encompassing the configurations of BH $M = Q$, $M > Q$, and $M < Q$. Furthermore, we also considered the modifications created by the Lorentz violation parameter l , the degree of nonlinearity of the electrodynamics γ , and the canonical and phantom configurations $\xi = \pm 1$.

In the second part of the work, we performed the light deflection calculation for the strong-field regime in order to analytically obtain the expressions for the expansion coefficients, aiming to control the logarithmic divergence that occurred in the limit where the impact parameter converges to the critical radius of the photon sphere and thus obtain the final expression for the angular deviation Eq. (39). From the equations obtained for the weak-field regime, we constructed the gravitational lensing expressions so that we could correlate these theoretical calculations with the observables associated with relativistic images. Due to technical difficulties, for the calculation of the angular position and radius of the Einstein ring, we considered only the expression for the deviation of light in spacetime from Kalb-Ramond Eq. (26) and considered only first-order terms in the mass M . For the strong-field regime, data relating to the BH at the center of our galaxy were used to calculate the angular deflection [37], and then we constructed some tables and graphs by varying the parameters, and then we can observe how these alter the observables. With regard to observables in the field regime, we use data from a bulge star [40] to verify how the radius of the Einstein ring and the angular position are modified with the variation of the Lorentz symmetry violation parameter.

ACKNOWLEDGMENTS

The authors express their gratitude for the fruitful discussions held with Professor Manuel E. Rodrigues. A. A. Araújo Filho is supported by Conselho Nacional de Desenvolvimento Científico e Tecnológico (CNPq) and Fundação de Apoio à Pesquisa do Estado da Paraíba (FAPESQ), project numbers 150223/2025-0 and 1951/2025. M. V. de S. Silva is supported by CNPq/PDE 200218/2025-5. R. L. L. Vitória is supported by Conselho Nacional de Desenvolvimento Científico e Tecnológico (CNPq) and by Universidade Estadual do Maranhão (UEMA), projects numbers 150420/2025-0 and by the EDITAL N. 102/2025-PPG/CPG/UEMA, respectively.

-
- [1] K. Schwarzschild. About the gravitational field of a mass point according to einstein's theory. *Berlin. Session Reports*, 18, 1916.
 - [2] R. Penrose. Gravitational collapse and space-time singularities. *Phys. Rev. Lett.*, 14:57–59, 1965.
 - [3] R. M. Wald. *General Relativity*. The University of Chicago Press, Chicago, 1984.
 - [4] R. D'Inverno. *Introducing Einstein's Relativity*. Oxford University Press, New York, 1998.
 - [5] Ke Yang, Yue-Zhe Chen, Zheng-Qiao Duan, and Ju-Ying Zhao. Static and spherically symmetric black holes in gravity with a background kalb-ramond field. *Physical Review D*, 108(12):124004, 2023.
 - [6] A. A Araújo Filho, J. A. A. S Reis, and H Hassanabadi. Exploring antisymmetric tensor effects on black hole shadows and quasinormal frequencies. *Journal of Cosmology and Astroparticle Physics*, 2024(05):029, 2024.
 - [7] Wen-Di Guo, Qin Tan, and Yu-Xiao Liu. Quasinormal modes and greybody factor of a lorentz-violating black hole. *Journal of Cosmology and Astroparticle Physics*, 2024(07):008, 2024.
 - [8] A. A. Araújo Filho. Particle creation and evaporation in Kalb-Ramond gravity. *JCAP*, 04:076, 2025.
 - [9] Ednaldo L. B Junior, José Tarciso S. S Junior, Francisco S. N Lobo, Manuel E Rodrigues, Diego Rubiera-Garcia, Luís F Dias da Silva, and Henrique A Vieira. Gravitational lensing of a schwarzschild-like black hole in kalb-ramond gravity. *Physical Review D*, 110(2):024077, 2024.
 - [10] Shokhzod Jumaniyozov, Saeed Ullah Khan, Javlon Rayimbaev, Ahmadjon Abdujabbarov, Sharofiddin Urinbaev, and Sardor Murodov. Circular motion and qpos near black holes in kalb-ramond gravity. *The European Physical Journal C*, 84(9):964, 2024.

- [11] Yu-Hao Jiang and Xuxin Zhang. Accretion of vlasov gas onto a black hole in the kalb–ramond field. *Chinese Physics C*, 2024.
- [12] A. A. Araújo Filho, N. Heidari, and Iarley P. Lobo. A non-commutative Kalb-Ramond black hole. *JCAP*, 09:076, 2025.
- [13] Zheng-Qiao Duan, Ju-Ying Zhao, and Ke Yang. Electrically charged black holes in gravity with a background kalb–ramond field. *The European Physical Journal C*, 84(8):798, 2024.
- [14] N Heidari, J. A. A. S Reis, H Hassanabadi, et al. The impact of an antisymmetric tensor on charged black holes: evaporation process, geodesics, deflection angle, scattering effects and quasinormal modes. *arXiv preprint arXiv:2404.10721*, 2024.
- [15] Ahmad al Badawi, Sanjar Shaymatov, and Izzet Sakalli. Geodesics structure and deflection angle of electrically charged black holes in gravity with a background Kalb–Ramond field. *Eur. Phys. J. C*, 84(8):825, 2024.
- [16] A. A Araújo Filho. Antisymmetric tensor influence on charged black hole lensing phenomena and time delay. *arXiv preprint arXiv:2406.11582*, 2024.
- [17] Muhammad Zahid, Javlon Rayimbaev, Nuriddin Kurbonov, Saidmuhammad Ahmedov, Chao Shen, and Ahmadjon Abdujabbarov. Electric Penrose, circular orbits and collisions of charged particles near charged black holes in Kalb–Ramond gravity. *Eur. Phys. J. C*, 84(7):706, 2024.
- [18] H. Chen, M. Y. Zhang, A. A. Araújo Filho, F. Hosseinifar, and H. Hassanabadi. Thermal, topological, and scattering effects of an AdS charged black hole with an antisymmetric tensor background. *Commun. Theor. Phys.*, 78(2):025404, 2026.
- [19] Wentao Liu, Di Wu, and Jieci Wang. Static neutral black holes in Kalb-Ramond gravity. *JCAP*, 09:017, 2024.
- [20] Jia-Zhou Liu, Shan-Ping Wu, Shao-Wen Wei, and Yu-Xiao Liu. Exact black hole solutions in gravity with a background Kalb-Ramond field. *JCAP*, 11:056, 2025.
- [21] Wentao Liu, Cuihong Wen, and Jieci Wang. Lorentz violation alleviates gravitationally induced entanglement degradation. *JHEP*, 01:184, 2025.
- [22] Yuxuan Shi, A. A. Araújo Filho, K. E. L. de Farias, V. B. Bezerra, and Amilcar R. Queiroz. Neutrino oscillations in a Kalb-Ramond black hole background. 12 2025.
- [23] Y. Sekhmani, A. Baruah, S. K. Maurya, J. Rayimbaev, M. Altanji, I. Ibragimov, and S. Muminov. Kalb-Ramond black holes sourced by ModMax electrodynamics: Some perturbative properties in the phantom sector. *Phys. Dark Univ.*, 50:102157, 2025.
- [24] B. Eslam Panah, B. Hamil, and Manuel E. Rodrigues. Topological Mod(A)Max AdS black holes. *Eur. Phys. J. C*, 86(1):81, 2026.
- [25] Erdem Sucu, Izzet Sakalli, and Emmanuel N. Saridakis. Branch structure and nonextensive

- thermodynamics of Kalb-Ramond-ModMax black holes: observational signatures. 1 2026.
- [26] Faizuddin Ahmed, Ahmad Al-Badawi, and Edilberto O. Silva. Observable Optical Signatures, Particle Dynamics and Epicyclic Frequencies of Mod(A)Max Black Holes. 2 2026.
- [27] Ahmad Al-Badawi, Faizuddin Ahmed, and İzzet Sakallı. Particle dynamics and thermal properties in Kalb–Ramond ModMax black holes: Theoretical predictions for observational tests of exotic physics. *Phys. Dark Univ.*, 50:102076, 2025.
- [28] Ednaldo L. B. Junior, Herlan N. Lemos, and Marcos V. de S. Silva. Tidal dynamics and stellar disruption in charged Kalb-Ramond black holes in nonlinear electrodynamics. 1 2026.
- [29] Manuel Barriola and Alexander Vilenkin. Gravitational field of a global monopole. *Phys. Rev. Lett.*, 63:341–343, Jul 1989.
- [30] Zheng-Qiao Duan, Ju-Ying Zhao, and Ke Yang. Electrically charged black holes in gravity with a background Kalb–Ramond field. *Eur. Phys. J. C*, 84(8):798, 2024.
- [31] Ednaldo L. B. Junior, José Tarciso S. S. Junior, Francisco S. N. Lobo, Manuel E. Rodrigues, Diego Rubiera-Garcia, Luís F. Dias da Silva, and Henrique A. Vieira. Gravitational lensing of a Schwarzschild-like black hole in Kalb-Ramond gravity. *Phys. Rev. D*, 110(2):024077, 2024.
- [32] Daniela S. J. Cordeiro, Ednaldo L. B. Junior, José Tarciso S. S. Junior, Francisco S. N. Lobo, Manuel E. Rodrigues, Diego Rubiera-Garcia, Luís F. Dias da Silva, and Henrique A. Vieira. Free-falling test particles in a charged Kalb-Ramond black hole: Gravitational Doppler effect and tidal forces. *Phys. Rev. D*, 112(10):104018, 2025.
- [33] V. Bozza. Gravitational lensing in the strong field limit. *Phys. Rev. D*, 66:103001, 2002.
- [34] Naoki Tsukamoto. Deflection angle in the strong deflection limit in a general asymptotically flat, static, spherically symmetric spacetime. *Phys. Rev. D*, 95(6):064035, 2017.
- [35] V. Bozza. Quasiequatorial gravitational lensing by spinning black holes in the strong field limit. *Phys. Rev. D*, 67:103006, 2003.
- [36] Samuel E. Vazquez and Ernesto P. Esteban. Strong field gravitational lensing by a Kerr black hole. *Nuovo Cim. B*, 119:489–519, 2004.
- [37] Reinhard Genzel, Frank Eisenhauer, and Stefan Gillessen. The Galactic Center Massive Black Hole and Nuclear Star Cluster. *Rev. Mod. Phys.*, 82:3121–3195, 2010.
- [38] A. R. Soares, C. F. S. Pereira, R. L. L. Vitória, and Erick Melo Rocha. Holonomy corrected Schwarzschild black hole lensing. *Phys. Rev. D*, 108(12):124024, 2023.
- [39] Cheongho Han and Andrew Gould. Einstein radii from binary source events. *Astrophys. J.*, 480:196, 1997.
- [40] F. Abe. Gravitational Microlensing by the Ellis Wormhole. *Astrophys. J.*, 725:787–793, 2010.
- [41] A. R. Soares, C. F. S. Pereira, R. L. L. Vitória, Marcos V. de S. Silva, and H. Belich. Light

deflection and gravitational lensing effects inspired by loop quantum gravity. *JCAP*, 06:034, 2025.